

Probing the sterile neutrino dipole portal with SN1987A and low-energy supernovae

Garv Chauhan^{1,*}, Shunsaku Horiuchi,^{1,2} Patrick Huber,¹ and Ian M. Shoemaker¹

¹*Center for Neutrino Physics, Department of Physics, Virginia Tech, Blacksburg, Virginia 24061, USA*

²*Kavli IPMU (WPI), UTIAS, The University of Tokyo, Kashiwa, Chiba 277-8583, Japan*



(Received 22 February 2024; accepted 7 June 2024; published 9 July 2024)

Beyond the Standard Model electromagnetic properties of neutrinos may lead to copious production of sterile neutrinos in the hot and dense core of a core-collapse supernova. In this work, we focus on the active-sterile transition magnetic moment portal for heavy sterile neutrinos. Firstly, we revisit the SN1987A cooling bounds for dipole portal using the integrated luminosity method, which yields more reliable results (especially in the trapping regime) compared to the previously explored via emissivity loss, also known as the Raffelt criterion. Secondly, we obtain strong bounds on the dipole coupling strength reaching as low as 10^{-11} GeV⁻¹ from energy deposition, i.e., constrained from the observation of explosion energies of underluminous Type IIP supernovae. In addition, we find that sterile neutrino production from Primakoff upscattering off of a proton dominates over scattering off of an electron for low sterile neutrino masses.

DOI: [10.1103/PhysRevD.110.015007](https://doi.org/10.1103/PhysRevD.110.015007)

I. INTRODUCTION

Neutrino flavor oscillations imply that neutrino masses are nonzero, a fact not accounted for in the Standard Model (SM). However, the observation of nonzero neutrino masses can be explained if the SM is augmented with at least two right-handed sterile neutrinos (for the two mass-splittings). In the absence of firm experimental guidance, we do not know how heavy, how many, or how interacting these sterile neutrinos are. As a result, a broad multiscale experimental and observational program is underway [1].

The most studied phenomenological setup for sterile neutrinos is to assume that their mass-mixing parameters are the keys to their production as well as detection. This is not however the only possibility. For example, there are well-motivated scenarios in which a relatively large transition dipole moment between active and sterile neutrinos dominates their behavior (e.g., [2–6]). A large phenomenological program has ensued to constrain active-sterile dipole moments by making use of an array of terrestrial, astrophysical, and cosmological data [3,5,7–30]. Lastly, we note that the possibility of neutrinos having nonzero magnetic moments has a long history, going back to Pauli’s letter in 1930 in which the neutrino was proposed as a new particle [31].

To date, some of the most sensitive probes of active-sterile dipole moments have involved supernovae (SNe) [6,12]. If their production is too frequent, they can lead to excessive cooling of SN1987A [12] or produce an overabundance of detectable neutrinos or photons [6]. However recently, low-energy supernovae have emerged as powerful probes of new physics [32,33]. In this paper, we will derive new constraints on active-sterile dipole moments from deposition of excess energy in low-energy supernovae, which is constrained from the observations of SN Type IIP light curves. We also revisit the SN1987A bounds in light of additional production modes, finding important differences with existing literature.

This paper is organized as follows. In Sec. II, we describe the various production modes of sterile neutrinos via the dipole interaction and compute their luminosity as a function of their mass and dipole coupling. In Sect. III, we discuss the observational constraints from SNe that allow us to impose constraints on active-sterile dipole moments. Finally in Sec. IV, we display our main results and discuss them in the context of the existing constraints on the dipole portal.

II. DIPOLE PORTAL AT SUPERNOVAE

After electroweak symmetry breaking, the effective Lagrangian for the dipole portal involving active-sterile transition magnetic moment can be written as

$$\mathcal{L} \supset i\bar{N}\not{\partial}N + \sum_{\alpha} d_{\alpha}\bar{N}\sigma_{\mu\nu}\nu_{L}^{\alpha}F^{\mu\nu} - \frac{M_N}{2}\bar{N}^cN + \text{h.c.} \quad (1)$$

where N is a sterile neutrino, ν_L is a SM left-handed neutrino field, $F^{\mu\nu}$ is the electromagnetic field strength

*gchauhan@vt.edu

Published by the American Physical Society under the terms of the [Creative Commons Attribution 4.0 International license](https://creativecommons.org/licenses/by/4.0/). Further distribution of this work must maintain attribution to the author(s) and the published article’s title, journal citation, and DOI. Funded by SCOAP³.

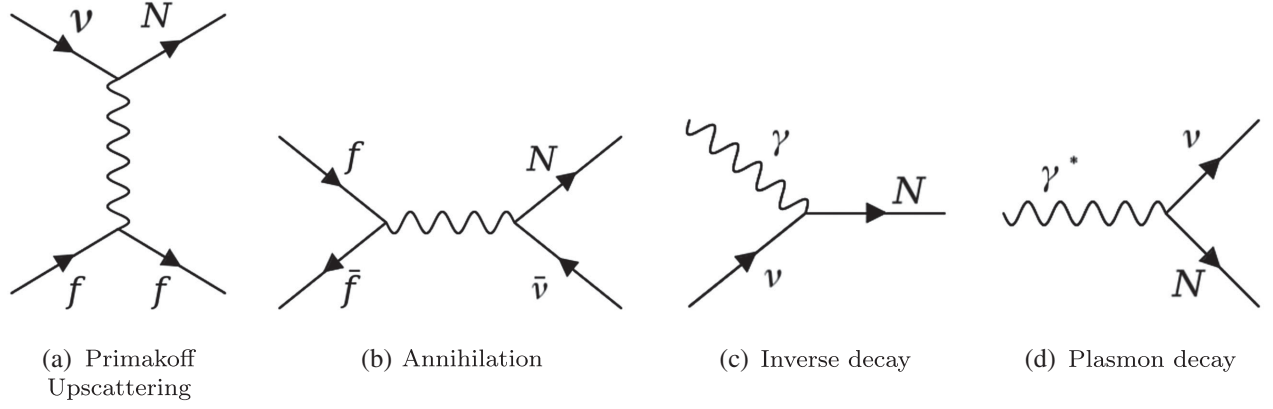


FIG. 1. Sterile neutrino production modes in SN through dipole portal via (a) Primakoff upscattering off a charged fermion via photon exchange, (b) charged fermion annihilation to a sterile and active neutrino, (c) photon + neutrino inverse decay, and (d) plasmon decay.

tensor, and d_α is the active-sterile transition magnetic moment. We assume the coupling strength to be flavor universal, i.e., $d_\alpha = d$. Note that we assume active and sterile neutrinos to be Majorana fermions. For specific UV scenarios explaining the origin of this coupling, see, e.g., Refs. [3,5,26,34,35].

A. Production

For a given active-sterile neutrino transition magnetic moment, heavy sterile neutrinos can be produced in a SN core through neutrino scattering off of electrons e^\pm , muons μ^\pm , and protons p , through pair annihilation of e^\pm or μ^\pm , inverse decay, and through plasmon decay (see Fig. 1). Despite the high number density, neutrons do not play any role in sterile neutrino production at the tree level. The relevant production modes are listed below [12]:

$$\nu + p \rightarrow N + p, \quad (\text{upscattering}) \quad (2)$$

$$\nu + e^\pm \rightarrow N + e^\pm, \quad (\text{upscattering}) \quad (3)$$

$$\nu + \mu^\pm \rightarrow N + \mu^\pm, \quad (\text{upscattering}) \quad (4)$$

$$e^+ + e^- \rightarrow \bar{\nu} + N, \quad (\text{annihilation}) \quad (5)$$

$$\mu^+ + \mu^- \rightarrow \bar{\nu} + N, \quad (\text{annihilation}) \quad (6)$$

$$\nu + \gamma \rightarrow N, \quad (\text{inverse decay}) \quad (7)$$

$$\gamma^* \rightarrow N + \bar{\nu}. \quad (\text{plasmon decay}) \quad (8)$$

The matrix elements for these processes have been calculated and provided in the appendix. In this work, we significantly improve on the production rate calculation in the literature by including the effect of muon population, plasmon decay channel, and the gravitational effects of the high-density proto-neutron star core. We also discuss and highlight a major result of our work: the dominance of

neutrino upscattering off of proton over upscattering through electron for low M_N .

Primakoff upscattering occurs through a t -channel exchange of a photon with the SN medium composed of protons, electrons, and muons. It can be seen in the matrix element for this process in Eq. (F1) prefers strong forward scattering. In vacuum, this diagram is regulated by restricting the angular range to forward scattering angles determined by the minimum momentum transfer required for sterile neutrino production in the final state [4,5,36]. However, in presence of a medium, the photon develops a nontrivial dispersion relation acquiring an effective plasmon mass, which can help regulate the total cross section. The effective mass of the transverse photon modes generally is of $\mathcal{O}(\omega_p)$, i.e., the plasma frequency. Including the contributions from electrons and protons in the SN medium, respectively, ω_p is given by

$$\omega_p^2 = \frac{4\alpha}{3\pi} \left(\mu_e^2 + \frac{\pi^2 T^2}{3} \right) + \frac{4\pi\alpha n_p}{m_p}, \quad (9)$$

where α is the fine-structure constant, μ_e is the electron chemical potential, T is the temperature of the SN core, and n_p and m_p are the number density and mass of the proton, respectively. Due to the high μ_e and high m_p ($\gg T$), ω_p is usually dominated by the relativistic electron plasma frequency (i.e., the first term). For typical $\mu_e \sim 250$ MeV, ω_p usually is of $\mathcal{O}(10$ MeV).

In addition, there is another screening length k_S determined by the *Debye-Hückel* scale k_D for nondegenerate nonrelativistic medium and by the *Thomas-Fermi* scale k_{TF} for degenerate medium. It arises from the movement of charged species in the medium, leading to charge screening of the target. The net screening scale including contributions from the proton and electrons, respectively, is given by

$$k_S^2 = \frac{4\pi\alpha}{T} n_p + \frac{4\alpha}{\pi} \left(\mu_e^2 + \frac{\pi^2 T^2}{3} \right), \quad (10)$$

where n denotes the number density of protons. Note that k_S doesn't suffer any suppression from the proton mass as compared to ω_p . Since highly degenerate and relativistic electrons in the SN core forms a stiff background, the dominant contribution to k_S comes from protons and other heavy ions. This can also be seen from Eq. (10); since $n_p \simeq n_e$ (charge neutrality) and $n_e = \mu_e^3/3\pi^2$ (degenerate fermi gas), the electron contribution in the second term is suppressed by a factor of T/μ_e .

From Eqs. (9) and (10), we can clearly see that $\omega_p < k_S$; i.e., charge screening tends to be the dominant scale. Hence, ignoring ω_p and considering photons to be massless is a good approximation for processes involving scattering off of charged targets, and k_S can help regulate the t -channel singularity. To include this screening effect for the Primakoff upscattering process, we make the following change to the matrix element:

$$|\mathcal{M}|^2 \rightarrow |\mathcal{M}|^2 \frac{q^4}{(q^2 - k_S^2)^2}, \quad (11)$$

where q^2 is the four-momentum carried by the photon propagator. Previously in the literature [12], a lower cutoff on q^2 was used, which is essentially equivalent to including a Debye screening effect in the matrix element, as shown in Eq. (11).

For any scattering involving the proton, the Dirac form factor $F_1(q^2)$ needs to be taken into account. We provide the relevant nuclear charge form factor in Appendix F, although for most q^2 of interest in our case, $F_1(q^2) \simeq 1$. Note that in this work, we neglect the effect of nucleon magnetic moments, and that will be included in a future study including the thermal effects for Primakoff upscattering.

The production through annihilation $f\bar{f} \rightarrow N\bar{\nu}$, where $f = e, \mu$, is shown in Fig. 1(b). Due to the s -channel exchange of a photon, this process does not suffer from the ‘‘forward’’ scattering issue encountered for Primakoff upscattering. Since there is also no scattering off charged species involved, the effect of the screening scale k_S is absent. The $|\mathcal{M}|^2$ for this process can be obtained by applying crossing symmetry rules to the (vacuum) matrix element for the Primakoff upscattering given in Eq. (F1).

Since the photons and neutrinos are thermalized in the SN core, the N production can also proceed through inverse decays $\gamma\nu \rightarrow N$ [see Fig. 1(c)]. The matrix element for this process is given in Eq. (D1). Usually, M_N up to $\sim 6T$ is accessible, but for ν_e with high chemical potential $\mu \gg 3T$, heavier N s can also be produced without significant Boltzmann suppression.

As discussed earlier, due to interactions with a high temperature and density medium, photons develop a thermal mass. Thus, the decays of photons also become

kinematically allowed in a SN core, as shown in Fig. 1(d). In our case, this mode is important only for sterile masses $M_N \lesssim \omega_p$. The decay rate is given in Eq. (E1) and detailed production rates are discussed later.

B. Boltzmann equations

The simplified kinetic equation for sterile neutrino production is

$$\frac{\partial f_N}{\partial t} = \mathcal{C}_{\text{coll}}(f_N), \quad (12)$$

where f_N is the sterile neutrino phase-space density distribution and $\mathcal{C}_{\text{coll}}$ is the sum of all possible collisional interactions. In our case, $\mathcal{C}_{\text{coll}}$ includes $2 \rightarrow 2$, $2 \rightarrow 1$ and $1 \rightarrow 2$ processes. The collisional term for $2 \rightarrow 2$ particle interactions can be written [37–41]

$$\begin{aligned} \mathcal{C}_{\text{coll}}(f_N) = & \frac{1}{2E_N} \int d^3\tilde{p}_2 d^3\tilde{p}_3 d^3\tilde{p}_4 \Lambda(f_N, f_2, f_3, f_4) \\ & \times |\mathcal{M}|_{12 \rightarrow 34}^2 \delta^4(p_N + p_2 - p_3 - p_4) (2\pi)^4, \end{aligned} \quad (13)$$

where $d^3\tilde{p}_i = d^3p_i / ((2\pi^3)2E_i)$, $\Lambda(f_N, f_2, f_3, f_4) = (1 - f_N)(1 - f_2)f_3f_4 - f_Nf_2(1 - f_3)(1 - f_4)$ is the phase-space factor including the Pauli blocking of final states, $|\mathcal{M}|^2$ is the interaction matrix element squared including the symmetry factor, and E_i and p_i are energy and momentum of the i th particle. The collisional integrals for $2 \rightarrow 1$ and $1 \rightarrow 2$ can be obtained similarly (see Appendices D and E).

For the N production rate, we assume the dipole strengths are weak enough to not affect the standard SN processes. We also set the initial distribution $f_N = 0$ since, for such range of $|d|$, the sterile neutrino produced will not be trapped and thermalized in the SN. After solving for f_N , we can calculate the differential luminosity as [37,41],

$$\frac{dL_N}{dE_N} = \frac{2E_N}{\pi} \int dr r^2 \frac{df_N}{dt} E_N p_N. \quad (14)$$

While the distribution functions for the leptons (l) have the usual Fermi-Dirac form determined by p_l, m_l, μ_l , and T , the case for nucleons is quite different due to strong interactions under high densities leading to the breakdown of noninteracting picture. The mean-field potentials arising from nucleon self-energies play an important role. In our case, they modify the dispersion relation for nucleons and significantly affect their Pauli-blocking factors. The dispersion relation for nucleons, considering them as a nonrelativistic quasiparticle gases moving under a mean-field potential U , is given [42,43]

$$E(\mathbf{p}) = \frac{\mathbf{p}^2}{2m^*} + m + U, \quad (15)$$

where m and m^* are the rest mass and Landau effective masses of the nucleon, respectively. m^* and U are both functions of temperature, density, and the neutron-to-proton ratio. Given the nucleon chemical potential (with rest mass included), we can now define the nucleon distribution function as

$$f_{\text{nucleon}}(p) = \frac{1}{\exp\left[\frac{\sqrt{p^2 + m^{*2}} - \mu^*}{T}\right] + 1}, \quad (16)$$

where we define the effective nucleon chemical potential $\mu^* = \mu - U$.

We can now define a useful concept for later discussions to quantify the degeneracy of Fermi gases. A Fermi gas is strongly degenerate when the chemical potential is greater than the average thermal energy. Therefore, the degeneracy parameter η_{deg} is defined as

$$\eta_{\text{deg}} = \frac{\mu - m}{T}. \quad (17)$$

Note for nucleons, we replace $\mu \rightarrow \mu^*$ and $m \rightarrow m^*$. Thus, $\eta_{\text{deg}} \gg 1$ is strongly degenerate, while $\eta_{\text{deg}} < 0$ is non-degenerate. For example, η_{deg} for the SN profile used in this work at postbounce time $t_{\text{pb}} = 1$ sec is shown in Fig. 2 (lower panel). While the electrons are strongly degenerate at all radii inside the SN core, the protons are only slightly degenerate in the center and turn nondegenerate at $r > 6$ km. The upper panel in Fig. 2 shows the filling factor for the momentum states for electrons and protons at $r = 2$ km ($t_{\text{pb}} = 1$ sec). We also include the case of strongly degenerate gas for comparison, assuming $\mu = \mu_e$ and $T \simeq 0$. Degeneracy has strong effects on the production rate. For example, the presence of highly degenerate species like electrons in the final state can suppress the production rate compared to the nondegenerate protons.

For the SN profile used in this work (details in the next section), Fig. 3 shows the different contributions to sterile neutrino luminosity L_N as functions of time. In Fig. 3(a), L_N is shown for all production modes listed in Eqs. (2)–(8) for $|d| = 10^{-9}$ GeV $^{-1}$ at $M_N = 10$ MeV. The proton Primakoff $\nu p \rightarrow N p$ is the dominant process for $M_N = 10$ MeV, with the rate of electron Primakoff $\nu e \rightarrow N e$ following closely. The bump around $t_{\text{pb}} = 9$ sec for electron Primakoff occurs due to numerical issues in discretizing the SN profile since the chemical potential for ν_e and ν_μ exhibit very sharp peaks for $t_{\text{pb}} \geq 9$ sec. Despite the same number densities as required by charge neutrality, the difference between the rates can arise from the high degeneracy of electrons, which lead to suppression of the production rate as compared to the proton case. The muon Primakoff is further suppressed due to the lower number density of muons, i.e., $n_\mu < n_e, n_p$. The rate from plasmon and inverse decay processes, although subdominant to

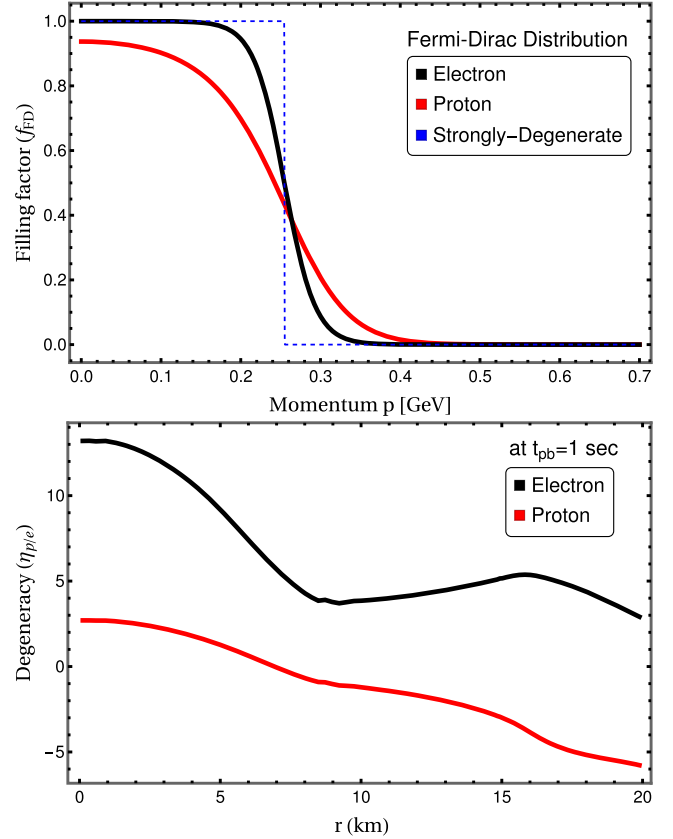


FIG. 2. (Upper panel) Fermi-Dirac distribution for three cases: proton, electron, and strongly degenerate gas at $r = 2$ km ($t_{\text{pb}} = 1$ sec). (Lower panel) Degeneracy parameter η_{deg} for e and p for our SN profile at $t_{\text{pb}} = 1$ sec.

Primakoff scattering, does not fall off as strongly as the kinematic limit is enhanced from the high-chemical potential of ν 's and due to the absence of Pauli blocking. In fact, even after chemical potentials drop between 8–10 sec, the average thermal energy of ν in $\nu\gamma \rightarrow N$ is sufficient for N production for low M_N . The production rate from annihilation channels $f\bar{f} \rightarrow N\nu$ are mainly determined by the chemical potentials μ_e and μ_μ . It can be seen from the SN profile that $\mu_e \sim \mu_\mu$ for most t_{pb} , thereby leading to the same production rate at most times. The overall magnitude of the annihilation rate is suppressed compared to the Primakoff process due to the suppressed number density of antifermions.

Similarly, in Fig. 3(b), L_N is shown for all relevant production modes for $M_N = 200$ MeV for $|d| = 10^{-9}$ GeV $^{-1}$. For heavier steriles, essentially all production modes will suffer severe Boltzmann suppression, especially at later times since temperatures and chemical potentials have dropped significantly by then. The rate for proton and electron Primakoff upscattering are quite similar (notice the log-scale for L_N) since the heavy sterile production cannot just proceed through scattering off the

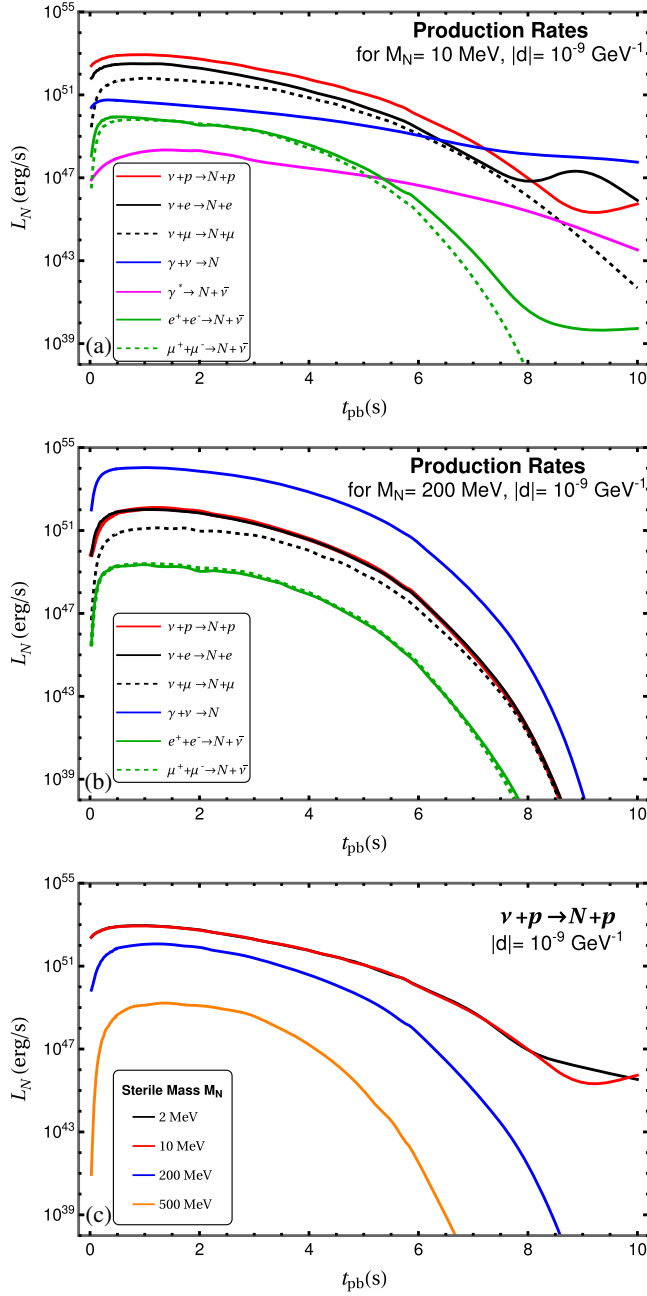


FIG. 3. Sterile neutrino luminosity as a function of time for $|d| = 10^{-9}$ GeV $^{-1}$ for (a) all production modes at $M_N = 10$ MeV, (b) all production modes at $M_N = 200$ MeV, and (c) proton Primakoff upscattering mode for different M_N .

Fermi surfaces only¹ and suppression from high degeneracy leads to exponential suppression. This also explains why the inverse decay dominates in this case. Since typical $\omega_p \ll 200$ MeV, the plasmon mode is absent in this case. Similar to the low M_N case, annihilation channels have

¹For light N , the initial f state has $E_f \sim \mu_e$ and can be placed back on the Fermi surface in the final state $\rightarrow f_{\text{nucleon}} = 1/2$, leading to no exponential suppression from degeneracy.

nearly the same rates due to similar chemical potentials μ_e and μ_μ .

In Fig. 3(c), L_N is shown for only the proton Primakoff upscattering process for different values of M_N at fixed $|d| = 10^{-9}$ GeV $^{-1}$. It can be seen that the production rates for low M_N are nearly equal. A dip around t_{pb} occurs for $M_N = 10$ MeV since that is the first instant when SN core temperatures dip below 10 MeV.

III. SUPERNOVAE BOUNDS

We discuss two different methods to obtain bounds on the dipole portal physics using SNe: (i) Raffelt criterion, and (ii) integrated luminosity (IL) criterion. While the former is a locally derived constraint on the energy lost by production of new particles, the latter is a global one.

The Raffelt criterion is applied at a characteristic radius and requires the local emissivity of the sterile neutrinos at r_0 to not exceed more than 10% of the total neutrino emissivity [12,36,44,45]; i.e.,

$$\frac{d\mathcal{E}_N}{dt}(r_0) \leq \frac{1}{10} \frac{d\mathcal{E}_\nu}{dt} \simeq \frac{\rho(r_0)}{g/\text{cm}^3} \times 10^{19} \text{ erg cm}^{-3} \text{ s}^{-1}. \quad (18)$$

For the integrated luminosity criterion, the energy-loss rate per unit mass can be converted to a total luminosity loss by taking the mass of the SN core and the duration of the SN event into account. Observations of energy-loss rate from SN1987A, assuming $M_{\text{core}} \sim 1M_\odot$, leads to the following upper bound:

$$E_{N,\text{cool}} < 10^{52} \text{ erg}. \quad (19)$$

Another class of constraint from SNe stems from the identification of a subclass of SNe with low explosion energies, termed underluminous Type IIP SNe. These have been recently used to constrain the parameter space of axions [46] and sterile neutrinos [33,47]. The explosion energy released in SNIIP explosions can be inferred from the spectrum and light curves. Using fitting formulas, simulations, and statistical inference, the lowest SNIIP explosion energies inferred is some 7.4×10^{49} [48–51]. Therefore, for our purposes, we assume the energy deposition from the decays of sterile neutrinos inside the SN envelope to be less than $E_{\text{dep}} < 10^{50}$ erg. Note that this energy deposition should occur beyond the radius of the SN core (R_{core}) but inside the envelope of the exploding star (R_{env}).

Previous works in the literature often employ the Raffelt criterion to set a cooling bound. Our results are in agreement with these when matching their assumptions, i.e., proton Primakoff scattering being subleading. We focus instead more on the IL bound. There are several advantages to the IL criterion. Firstly, it is more consistent with the physical picture of the process; i.e., sterile neutrino

production occurs at different times and at different radii throughout the proto-neutron star core. Secondly, as we will show later, the Raffelt criterion is not reliable to obtain bounds in the trapping regime. Since it assumes the sterile neutrino production at a specified radius, the absorption rate might be dominated by other modes apart from decays. It will be demonstrated later using IL criterion that the bounds in the trapping regime are set by the sterile neutrino decay rather than scatterings. Hence, for heavy sterile neutrinos that can decay, the IL criterion is more apt.

For our purposes, we assume N production through very small transition magnetic moments do not appreciably affect the standard SN processes. In this work, we apply our reasoning to obtain bounds in the dipole coupling—mass plane with the SFHo-18.8 model simulated by the Garching group, which adopts a $18.8M_{\odot}$ progenitor and includes six-species neutrino transport [43,52,53]. We use the simulated SN evolution assuming $R_{\text{core}} \sim 20$ km for all postbounce time sequences up to ~ 10 s and assume an envelope extending up to $\sim 5 \times 10^8$ km.

A. Absorption modes

The decay and scatterings of N can lead to novel energy deposition in the SN envelope, which can contribute to the SN explosion. The relevant processes that determine the mean free path are

$$N + e^{\pm} \rightarrow \nu + e^{\pm}, \quad (\text{downscattering}) \quad (20)$$

$$N + \mu^{\pm} \rightarrow \nu + \mu^{\pm}, \quad (\text{downscattering}) \quad (21)$$

$$N + p \rightarrow \nu + p, \quad (\text{downscattering}) \quad (22)$$

$$N + \bar{\nu} \rightarrow \gamma, \quad (\text{annihilation}) \quad (23)$$

$$N \rightarrow \nu + \gamma. \quad (\text{decay}) \quad (24)$$

In the absence of scatterings, the decay rate Γ is dominated by the $N \rightarrow \nu + \gamma$ process, for which the vacuum decay rate is given by

$$\Gamma_{N \rightarrow \nu + \gamma} = \frac{d^2 M_N^3}{4\pi}. \quad (25)$$

The decay length λ_{decay} can be calculated by taking the Lorentz factor $\gamma = 1/\sqrt{1-\beta^2}$ into account; i.e., $\lambda_{\text{decay}} = \gamma\beta/\Gamma_{N \rightarrow \nu + \gamma}$, where $\beta = p_N/E_N$. Due to the significant population of photons and neutrinos inside the SN core, the decay rate for radiative decay will be modified. This difference occurs because of Pauli blocking of neutrinos and stimulated emission of the photon (bose enhancement) in the final state. The mean free path calculation including these effects will be described in detail later.

Note that similar to our work in [33], we assume that a major portion of the outgoing energy in scattering and decay processes is carried by non-neutrino species, which are readily absorbed by the SN medium. We also point out that high-energy neutrinos are most likely to be deposited. Hence, it is a good assumption that entire energy of the downscattered or decayed N is deposited inside the SN.

B. Energy cooling/deposition

Our constraints arise from the sterile neutrino production in the SN core through the magnetic moment portal, with the bounds on the energy loss or deposition arising from observations of SN1987A and low-energy SNIIP, respectively. The salient details of the production processes have been discussed in previous sections. The total energy deposited or taken away ($E_{\text{dep/cool}}$) from the SN core can be calculated by time integrating the differential sterile neutrino luminosity L_N over the core volume, weighted by the escape probability $P_{\text{cool/dep}}$

$$E_{\text{dep/cool}} = \eta_{\text{lapse}}^2 \int dt \int_0^{R_{\text{core}}} dr \int_{M_N}^{\infty} dE_N \frac{dL_N(r, E_N, t)}{dr dE_N} \times \Theta\left(E_N - \frac{M_N}{\eta_{\text{lapse}}}\right) \times P_{\text{cool/dep}}(r), \quad (26)$$

where η_{lapse} is the gravitational redshift factor, E_N is the sterile neutrino energy, $\frac{dL_N(r, E_N, t)}{dr dE_N}$ is the gradient of the differential sterile neutrino luminosity, $\Theta(x)$ is the Heaviside theta function, and $P_{\text{cool/dep}}(r)$ is the probability for N produced at r to escape. $P_{\text{cool/dep}}$ is determined by the mean free path of the sterile neutrino in the hot dense environment of the SN. $P_{\text{cool/dep}}$ incorporates the effect of the decays and scattering of the sterile neutrino with the medium, which might prohibit the efficient transport of the energy from the core to mantle and/or beyond. Using the absorptive width of the sterile neutrino Γ_{abs} , we can define P_{cool} in terms of the optical depth τ [54],

$$P_{\text{cool}}(r) = \exp[-\tau(r, R)] = \exp\left[-\int_r^R \Gamma_{\text{abs}}(r') dr'\right]. \quad (27)$$

The absorption rate for $2 \rightarrow 2$ scatterings is given by an expression similar to the collisional term [54–56],

$$\Gamma_{\text{abs}} = \frac{1}{2p_N} \int d^3 \tilde{p}_2 d^3 \tilde{p}_3 d^3 \tilde{p}_4 \tilde{\Lambda}(f_2, f_3, f_4) \times |M|_{12 \rightarrow 34}^2 \delta^4(p_N + p_2 - p_3 - p_4) (2\pi)^4, \quad (28)$$

where $\tilde{\Lambda}(f_2, f_3, f_4) = f_2(1-f_3)(1-f_4)$.

The cooling bound is applicable only if the energy from the core can be transferred efficiently beyond the shock, where this energy cannot be reprocessed for neutrino production/streaming. For example, N might decay before

the shock radius, which will not lead to an energy loss, and the cooling bound will not apply. The average probability for the energy transport beyond the neutrinosphere is given by

$$P_{\text{cool}}^{\text{SN1987A}}(r) = \exp \left[- \int_r^{R_{\text{far}}} \Gamma_{\text{abs}}(r') dr' \right]. \quad (29)$$

Note that we assume radial outward propagation for the calculation of the absorptive width. R_{far} can be defined in two different ways with the only strict requirement being $R_{\text{far}} > R_\nu$. Usually R_{far} is not set very close to R_ν since the production rate from the outermost thin shell centred at R_ν might be overestimated. Note that the actual position of R_{far} is inconsequential for the bounds derived in our work as long as it is beyond the neutrinosphere since the optical depth is dominated by the absorptive width of the high temperature region surrounding the radius of the production especially the regions just beyond R_{core} if the final state in the decays or scatterings is Pauli blocked inside the core. In the literature, either radius $R \sim \mathcal{O}(100)$ km or $\sim \mathcal{O}(1000)$ km (the latter being the shock radius) is usually chosen as representative values for R_{far} [54]. In this work, we set R_{far} to $\sim \mathcal{O}(100)$ km.

For the case of low-energy SN, the bounds apply only if energy deposition takes place between R_{core} and the outermost envelope radius, R_{env} . Therefore, the escape probability in this case can be written

$$P_{\text{dep}}^{\text{SN1987A}}(r) = \exp \left[- \int_r^{R_{\text{core}}} \Gamma_{\text{abs}}(r') dr' \right] \times \left(1 - \exp \left[- \int_{R_{\text{core}}}^{R_{\text{env}}} \Gamma_{\text{abs}}(r') dr' \right] \right). \quad (30)$$

For our purposes, R_{core} can be defined as the radius of the neutrinosphere beyond which neutrinos free stream, broadly defined as the radius at which T_{SN} falls down to 3 MeV. The actual neutrinosphere radius depends on the neutrino flavor, but assuming the same R_ν for all species will not affect the bound appreciably. In this work, $R_{\text{core}} = 20$ km, and R_{env} is chosen to be the progenitor radius equal to 5×10^{13} cm.

We also include the effect of gravitational trapping. In the absence of sufficient kinetic energy, the presence of high matter densities can lead to sterile neutrino getting trapped. Therefore, it is required that $E_N > m_s/\eta_{\text{lapse}}$, where η_{lapse} relates the energy measured in the SN frame to the energy measured by an observer at infinity. We also need to account for gravitational time dilation, which corrects for the time interval measured locally compared to an observer at infinity. Therefore, a factor of η_{lapse} for L_N and another factor for the time interval dt leads to the prefactor η_{lapse}^2 in Eq. (26).

IV. RESULTS AND DISCUSSION

We display our main results in Fig. 4 for flavor universal active-sterile magnetic moment as a function of sterile neutrino mass M_N . The curves shown in blue are obtained through the SN1987A cooling bound $E_{N,\text{cool}} < 10^{52}$ erg.

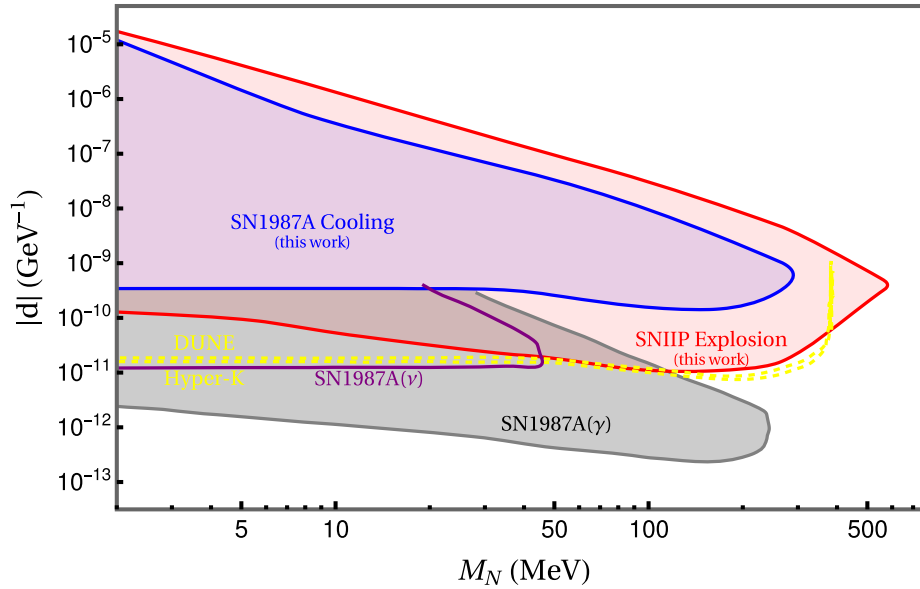


FIG. 4. Bounds on flavor universal dipole strength $|d|$ from SN1987A cooling (blue) and SNIIP explosion energies (red) as functions of sterile neutrino mass. Other displayed constraints include SN1987A(γ) [6], SN1987A(ν) [6] and the experimental sensitivity of DUNE and Hyper-K for a future Galactic SN at a distance of 10 kpc [6].

The curves shown in red are obtained through the bound on explosion energies using SNIIP, $E_{N,\text{dep}} < 10^{50}$ erg. The bound from SNIIPs is almost an order of magnitude stronger than the cooling bound. It can reach $|d|$ as low as 10^{-11} GeV $^{-1}$ and provides one of the leading constraint for $30 \text{ MeV} \leq M_N \leq 600 \text{ MeV}$. We also include other constraints on $|d|$ from the radiative decay of N from SN1987A [6] (labeled SN1987A(γ)) and from the bound on the neutrino flux arising from radiative decay [6] (labeled SN1987A(ν)). The dotted yellow curve shows the experimental sensitivity of upcoming neutrino experiments DUNE and Hyper-Kamiokande for a future galactic SN, assuming a hypothetical distance of $D_{SN} = 10$ kpc [6].

In the bottom region of the blue and red curves, the production rate for low M_N is dominated by proton Primakoff upscattering, followed by the electron upscattering [also see Fig. 3(a)]. The production rate for Primakoff upscattering for low M_N is largely independent of M_N as also indicated by the flat region in the cooling bound curve. Upon increasing M_N , the inverse decay starts to dominate the production rate, especially above 50 MeV. The inverse decay production rate depends on M_N^4 and remains dominant up to the kinematic threshold of $\sim \mu_{\nu_e} + T$ but suffers Boltzmann suppression above these masses. Since the couplings are extremely low in this regime, the exponential factor $P_{\text{esc}} \simeq 1$ in this region.

For the trapping regime, the coupling is set by the requirement that the mean free path length is less than $\mathcal{O}(R_{\text{core}})$. In this region, the couplings are really high, and therefore, production regions with higher absorption rates get suppressed in the energy integral [Eq. (26)]. Therefore, the dominant contribution arises from regions with the least absorption rates, i.e., regions near R_{core} . In these outer regions near the core, the proton and electron number density are comparatively lower; therefore, the absorption rate is dominated by the decays of N , which sets the maximum allowed coupling strength in the trapping regime. This is in direct contrast to the Raffelt criterion where the opacity is calculated at a given radius only, and if chosen inside the core, the absorption rate might be dominated by other modes as also implemented by Ref. [12]. They find the Primakoff upscattering contribution to the absorption rate to be dominant, which leads to the flattening of the trapping bound at low M_N , which, however, is not the correct physical picture as pointed above. A brief discussion and comparison of their results with ours is presented in Appendix A. Another important observation is the impact of the broadness of the sterile neutrino energy spectrum. For a broader energy spectrum (e.g., in Fig. 5), higher energy N 's can be produced at a similar rate as compared to the assumed mean sterile neutrino energy (see Ref. [12]). To trap these energetic N 's, the couplings need to be comparatively higher, which results in the trapping regime shifting to higher values. This is the primary reason why our trapping bound for higher

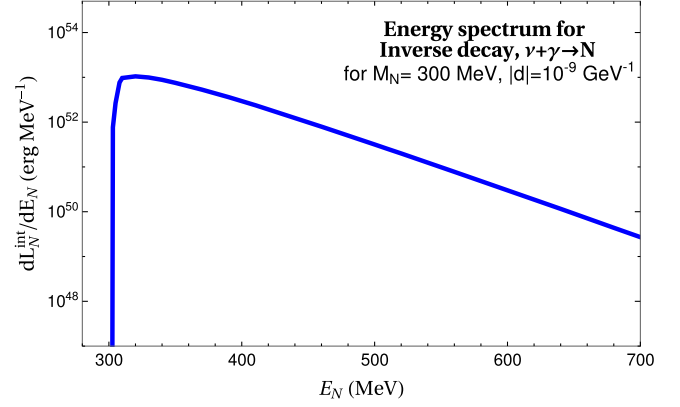


FIG. 5. Differential time-integrated luminosity as a function of sterile neutrino energy for $M_N = 300$ MeV and $|d| = 10^{-9}$ GeV $^{-1}$ for inverse decay process.

masses assuming R_{far} at $r = 100$ km matches Ref.'s [12] bound, which assumes R_{far} at $r = 25$ km.

We also point out that our results are consistent with the cooling bound constraint in Ref. [6] using $8.8M_{\odot}$ progenitor. However, Ref. [6] did not include the proton upscattering mode. In addition, the progenitor star for SN1987A is more than likely approximated by a $18.8M_{\odot}$ progenitor than a $8.8M_{\odot}$, the latter of which tends to have lower maximum temperatures, which especially affects the thermal production of N at high M_N through inverse decays.

The magnetic moment portal, although quite similar at first glance to the axion case [32] (both species with radiative couplings), differ qualitatively from each other. In the former case, the production rate is enhanced especially for lower M_N from the high chemical potential of ν in the initial state, for both Primakoff upscattering and inverse decay processes, while no such enhancement is possible for the axion case, where the ν is replaced by the γ , which is thermally produced.

V. CONCLUSIONS

We have revisited the SN1987A cooling bound and obtained new bounds from SNIIP explosion energies for the dipole portal. We found that SNe can be efficient sites of sterile neutrino production via magnetic moments and that the integrated luminosity criteria can produce stronger results than the Raffelt criterion, especially in the trapping regime. Secondly, we have found that low-energy supernovae can significantly cover previously unconstrained parameter space.

We have included the effect of nucleon self-energies, Debye screening, and gravitational trapping, as well as the effect of degeneracy on the production rates. In addition to including the plasmon decay channel, our work also includes the production modes arising from substantial muon population in the SNe core.

Future directions for this work motivates the calculation of exact thermal rates for Primakoff upscattering. In light of proton Primakoff upscattering rate, the constraints derived from the neutrino and photon flux arising from the radiative decay of N from SN1987A might become stronger [6]. Another interesting case might occur: The γ from low mass steriles decaying outside the SN might not be able to escape and could form a fireball, like in the case of axions [57,58]. In addition, the bounds may be improved by refined calculation for the thermalization and trapping of N 's, accounting for their nonoutward radial propagation [59] and including thermal masses of photons in N decays.

The SNIIP bound could be improved even further in future if progenitors with even smaller explosion energies than 10^{50} erg are observed. Also, currently, the SNIIP bound is conservative since we have entirely ignored the contribution of the standard processes to the explosion energy. Therefore, these bounds can also be improved if these contributions are known more precisely, through a detailed comparison of the simulated vs observed SNIIP explosions.

ACKNOWLEDGMENTS

We are very grateful to Vedran Brdar, Ryan Plestid, Yingying Li, Damiano Fiorillo, and Edoardo Vitagliano for helpful discussions. We thank Hans-Thomas Janka and Daniel Kresse for providing the SN profiles used in this work. G. C. would like to also thank Washington University physics department for the use of HPC Center facilities. The work of G. C., S. H., P. H., and I. S. is supported by the U.S. Department of Energy under the Award No. DE-SC0020250 and DE-SC0020262. The work of S. H. is also supported by NSF Grant No. AST1908960 and No. PHY-2209420, and JSPS KAKENHI Grant Number JP22K03630 and JP23H04899. This work was supported by the World Premier International Research Center Initiative (WPI Initiative), MEXT, Japan.

APPENDIX A: COMPARISON WITH RAFFELT CRITERION

We will compare and discuss the results for cooling bound for the dipole portal obtained in Ref. [12] with our results using the Raffelt criterion for the same $18.8M_{\odot}$ progenitor [60] at $r = 14$ km, shown in Fig. 6. As detailed in Ref. [12], their cooling bound (blue curve) is dominated by the electron Primakoff upscattering for lower M_N and by inverse decays for higher M_N . For faithful comparison, we show our results for cooling bound excluding the proton upscattering mode, shown as a solid red curve. It can be clearly seen that our results are in complete agreement by excluding the upscattering off of proton. However, upon including the proton upscattering process, the cooling bound becomes stronger as shown in dashed red curve.

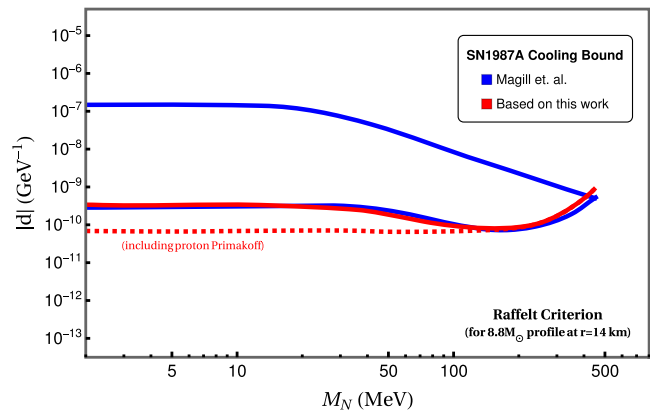


FIG. 6. SN1987A cooling bound obtained using the Raffelt criterion in Refs. [12] (blue curve) and using the production rate calculation used in this work (red curve; for details, refer to text). The dashed red line shows bounds using the Raffelt criterion including proton Primakoff upscattering.

Therefore, we observe that the proton mode can help improve the constraint on the dipole portal.

As for the cooling bound in the trapping regime (as discussed earlier in Sec. IV), since the Raffelt criterion is done at a specified radius, usually at $r < R_{\text{core}}$, the opacity calculation to obtain bounds does not capture the real picture. Assuming a monoenergetic sterile neutrino for trapping also affects the analysis. It only becomes clear in the implementation of integrated luminosity criterion that production rate at very high couplings in spite of the high absorption rate can still proceed from the edges of the core; therefore, cooling/trapping bound is still applicable since at $r \sim R_{\text{core}}$, the dominant channel for energy loss/deposition is the sterile neutrino decay. Therefore, N decays set the trapping regime for all M_N irrespective of the other scattering modes.

APPENDIX B: EFFECT OF GRAVITATIONAL TRAPPING

In our work, we also include the effect of gravitational trapping. In Fig. 7, the dashed blue and red curves are bounds from cooling and explosion energies, respectively, but without taking the effect of gravitational trapping into account. We observe that for the SN1987A cooling bound, gravitational effects lead to trapping of $M_N \gtrsim 300$ MeV, while for the SNIIP explosion bound, although the M_N range is not affected appreciably, the bounds for higher M_N become weaker. This occurs due to gravitational trapping leading to a suppression of production rates, which can only be countered through increased coupling strength for the cooling or explosion energy bound to apply. However, increased $|d|$ required for the cooling case is beyond the trapping regime; therefore, gravitational effects shrink the mass reach of the cooling bound.

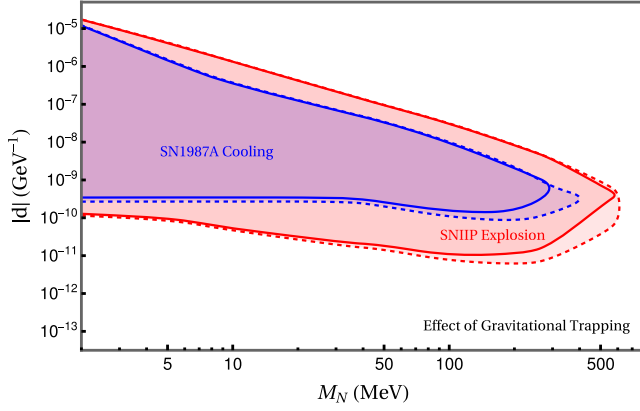


FIG. 7. Comparison of the effect of gravitational trapping on the bounds obtained from SN1987A cooling (blue) and SNIIP explosion energies (red). Dashed curved correspond to the case of no gravitational trapping.

APPENDIX C: COLLISIONAL INTEGRAL FOR S -CHANNEL PROCESS

For s -channel processes, the standard reduction of nine-dimensional collisional term to a three-dimensional integral as detailed in Ref. [38] fails. This happens due to the momentum transfer q^2 in the denominator for the matrix element of the s -channel process being a function of $\cos \alpha$. Due to which the usual step involving analytical integration of $\cos \alpha$ does not work. In this Appendix, we show how the integrals in Eq. (13) can be reduced from nine to three dimensions for a s -channel process. Our procedure closely follows the techniques used in Ref. [38]. Our procedure primarily relies on swapping out the angular coordinates for \mathbf{p}_2 and \mathbf{p}_3 compared to the standard way. Note that this simple change leads to nontrivial sign and variable changes throughout the standard calculation; therefore, we reproduce our entire calculation here. We begin by using the following property:

$$\cos \beta_i = \frac{2E_2E_3 - 2p_2p_3 \cos \alpha \cos \theta - Q - 2E_1E_2 + 2p_1p_2 \cos \theta + 2E_1E_3 - 2p_1p_3 \cos \alpha}{2p_2p_3 \sin \alpha \sin \theta}, \quad (\text{C9})$$

and $Q \equiv m_1^2 + m_2^2 + m_3^2 - m_4^2$. To account for the two different solutions for $\cos \beta$, we can restrict the integration interval to $[0, \pi]$ and multiply with a factor of 2. Note that since the integrand is independent of μ , the integration over $d\mu$ is trivial and equals 2π .

The limits of integration in $d \cos \alpha$ come from demanding that $\cos^2 \beta \leq 1$. This requirement can also be stated as

$$\frac{d^3 p_4}{2E_4} = d^4 p_4 \delta(p_4^2 - m_4^2) \Theta(p_4^0). \quad (\text{C1})$$

The integral over p_4 is done using the four-dimensional delta function arising from momentum conservation in the scattering process, enforcing $p_4 = p_1 + p_2 - p_3$ throughout rest of the calculation. We now introduce the following spherical coordinates for the three-momenta,

$$\mathbf{p}_1 = p_1(0, 0, 1), \quad (\text{C2})$$

$$\mathbf{p}_2 = p_2(0, \sin \theta, \cos \theta), \quad (\text{C3})$$

$$\mathbf{p}_3 = p_3(\sin \alpha \sin \beta, \sin \alpha \cos \beta, \cos \alpha). \quad (\text{C4})$$

The volume element for p_2 and p_3 can be written as

$$d^3 p_2 = p_2^2 dp_2 d \cos \theta d\mu, \quad (\text{C5})$$

$$d^3 p_3 = p_3^2 dp_3 d \cos \alpha d\beta, \quad (\text{C6})$$

with μ and β being the azimuthal angles for \mathbf{p}_2 and \mathbf{p}_3 . The integration over $d\beta$ is carried out using $\delta(p_4^2 - m_4^2) \equiv \delta(f(\beta))$, by using the relation

$$\int d\beta \delta(f(\beta)) = \sum_i \int d\beta \frac{1}{|f'(\beta)|_{\beta=\beta_i}} \delta(\beta - \beta_i), \quad (\text{C7})$$

where the β_i are the roots of $f(\beta) = 0$ and

$$f'(\beta) = \frac{df(\beta)}{d\beta} = -2p_2p_3 \sin \alpha \sin \theta \sin \beta, \quad (\text{C8})$$

with $\sin \beta_i = \pm(1 - \cos^2 \beta_i)^{1/2}$, where

$$(f'(\beta))^2 = (2p_2p_3 \sin \alpha \sin \theta \sin \beta)^2 \geq 0. \quad (\text{C10})$$

Therefore, we can write

$$\int_0^{2\pi} d\beta \delta(f(\beta)) = 2 \frac{1}{|f'(\beta)|_{\beta=\beta_i}} \Theta(|f'(\beta)|_{\beta=\beta_i}^2). \quad (\text{C11})$$

To simplify the expressions, we introduce the following definitions:

$$\begin{aligned}
 \gamma &= E_1 E_2 - E_1 E_3 - E_2 E_3; \\
 \epsilon &= -p_1 p_2 \cos \theta; \\
 k &= p_1^2 + p_2^2; \\
 a &= p_3^2(-4k + 8\epsilon); \\
 b &= -p_3(p_1 - \epsilon/p_1)(8\gamma + 4Q + 8\epsilon); \\
 c &= -4\gamma^2 - 4\gamma Q - Q^2 - 8\gamma\epsilon - 4Q\epsilon - 4\epsilon^2 \\
 &\quad + 4p_2^2 p_3^2(1 - \cos^2 \theta).
 \end{aligned}$$

With the above notation, $f'(\beta)$ can be written as

$$|f'(\beta)|_{\beta=\beta_i} = \sqrt{a \cos^2 \alpha + b \cos \alpha + c}. \quad (\text{C12})$$

All possible matrix elements only include products of the four-momenta, which are calculated below:

$$\begin{aligned}
 p_1 \cdot p_2 &= E_1 E_2 - p_1 p_2 \cos \theta, \\
 p_1 \cdot p_3 &= E_1 E_3 - p_1 p_3 \cos \alpha, \\
 p_1 \cdot p_4 &= m_1^2 + (E_1 E_2 - p_1 p_2 \cos \theta) - (E_1 E_3 - p_1 p_3 \cos \alpha), \\
 p_2 \cdot p_3 &= (E_1 E_2 - p_1 p_2 \cos \theta) - (E_1 E_3 - p_1 p_3 \cos \alpha) + \frac{Q}{2}, \\
 p_2 \cdot p_4 &= (E_1 E_3 - p_1 p_3 \cos \alpha) + m_2^2 - \frac{Q}{2} \\
 p_3 \cdot p_4 &= (E_1 E_2 - p_1 p_2 \cos \theta) - m_3^2 + \frac{Q}{2}.
 \end{aligned}$$

Now it can be checked that all s -channel processes are analytically integrable over $d \cos \alpha$ and can be carried out by using these relations [39]:

$$\begin{aligned}
 &\int \frac{1}{\sqrt{ax^2 + bx + c}} \Theta(ax^2 + bx + c) dx \\
 &= \frac{\pi}{\sqrt{-a}} \Theta(b^2 - 4ac); \\
 &\int \frac{x}{\sqrt{ax^2 + bx + c}} \Theta(ax^2 + bx + c) dx \\
 &= -\frac{b}{2a} \frac{\pi}{\sqrt{-a}} \Theta(b^2 - 4ac); \\
 &\int \frac{x^2}{\sqrt{ax^2 + bx + c}} \Theta(ax^2 + bx + c) dx \\
 &= \left(\frac{3b^2}{8a^2} - \frac{c}{2a} \right) \frac{\pi}{\sqrt{-a}} \Theta(b^2 - 4ac).
 \end{aligned}$$

The step function arises from demanding a real integration interval. This also ensures that the roots of $ax^2 + bx + c$ are not outside the fundamental integration interval of $[-1, 1]$. Similarly, the integration interval for

integration over $d \cos \theta$ is given by the solutions of $b^2 - 4ac = 0$:

$$\cos \theta = \frac{2\gamma + 2p_3^2 + Q \pm 2p_3 \sqrt{2\gamma + p_1^2 + p_2^2 + p_3^2 + Q}}{2p_1 p_2}. \quad (\text{C13})$$

For the integration interval to be real, both of these solutions are required to be real. We refer to these two solutions as $\cos \theta_-$ and $\cos \theta_+$. The real integration limits are $\alpha = \sup[-1, \cos \theta_-]$ and $\beta = \inf[+1, \cos \theta_+]$ with $\alpha \leq \beta$. Finally, by combining all the analytical simplifications described above, Eq. (13) is reduced to the following three-dimensional integral, which is evaluated numerically:

$$\begin{aligned}
 C_{\text{coll}}(f_1) &= \frac{2}{(2\pi)^4} \frac{1}{2E_1} \int_0^\infty \int_0^{p_1+p_2} \int_\alpha^\beta d \cos \theta \frac{p_2^2 d p_2 p_3^2 d p_3}{2E_2^2 2E_3} \\
 &\quad \times \Lambda(f_1, f_2, f_3, f_4) F(p_1, p_2, p_3) \Theta(A), \quad (\text{C14})
 \end{aligned}$$

where A is the parameter space allowed; i.e., $\alpha, \beta \in \mathbb{R}$, $\alpha \leq \beta$, and F is derived from the following analytical integral:

$$\begin{aligned}
 F(p_1, p_2, p_3) &\equiv \int \frac{|M|^2}{\sqrt{a \cos^2 \alpha + b \cos \alpha + c}} \\
 &\quad \times \Theta(a \cos^2 \alpha + b \cos \alpha + c) d \cos \alpha. \quad (\text{C15})
 \end{aligned}$$

APPENDIX D: COLLISIONAL INTEGRAL FOR $N \leftrightarrow \nu + \gamma$

The matrix element for the decay process $N \rightarrow \nu + \gamma$ is

$$|\mathcal{M}|^2 = 2d^2(M_N^2 - m_\nu^2)^2. \quad (\text{D1})$$

The collision term for $2 \rightarrow 1$ inverse decay in this case is [54,56]

$$\begin{aligned}
 C_{\nu+\gamma \rightarrow N} &= \frac{1}{2E_N} \int \frac{d^3 p_\gamma}{(2\pi^3) 2E_\gamma} \frac{d^3 p_\nu}{(2\pi^3) 2E_\nu} f_\gamma(E_\gamma) f_\nu(E_\nu) \\
 &\quad \times |\mathcal{M}|_{N \rightarrow \nu+\gamma}^2 \delta^4(p_N - p_\gamma - p_\nu) (2\pi)^4, \quad (\text{D2})
 \end{aligned}$$

where $f_i(E)$ is the respective quantum-statistics factor, i.e., Bose-Einstein or Fermi-Dirac, for the initial states. The above six-dimensional integral can be reduced to the following one-dimensional integral:

$$\begin{aligned}
 C_{\nu+\gamma \rightarrow N} &= \frac{d^2 M_N^4}{16\pi p_N E_N} \int_{P^-}^{P^+} d p_\gamma f_\gamma(p_\gamma) \\
 &\quad \times f_\nu \left(\sqrt{p_N^2 + M_N^2 - p_\gamma} \right), \quad (\text{D3})
 \end{aligned}$$

where $P^\pm = (E_N \pm p_N)/2$.

Similarly, the absorption rate Γ in a medium composed of photons and neutrinos can be written as

$$\Gamma_{N \rightarrow \nu + \gamma} = \frac{d^2 M_N^4}{16\pi p_N^2} \int_{p^-}^{p^+} dp_\gamma (1 + f_\gamma(p_\gamma)) \times \left[1 - f_\nu \left(\sqrt{p_N^2 + M_N^2} - p_\gamma \right) \right]. \quad (\text{D4})$$

In absence of a medium, the thermal distributions vanish and yield the vacuum decay rate. This difference occurs because of Pauli blocking of neutrinos, i.e., $(1 - f_\nu(E))$, and stimulated emission of the photon (bose enhancement), i.e., $(1 + f_\gamma(E))$ in the final state.

APPENDIX E: PLASMON DECAY

The decay rate for $\gamma^* \rightarrow N + \bar{\nu}$, applicable to both transverse and longitudinal excitations, is given by [5,61]

$$\Gamma_{\gamma^*} = \frac{d^2}{24\pi} \mathcal{Z} \frac{(\omega^2 - k^2)^2}{\omega} \left(1 - \frac{M_N^2}{K^2} \right)^2 \times \left(1 + 2 \frac{M_N^2}{K^2} \right) \Theta(K - M_N), \quad (\text{E1})$$

where \mathcal{Z} is the renormalization constant, $K^2 = \omega^2 - k^2$ is the effective plasmon mass, ω and k are plasmon energy and momentum.

The total energy loss rate including contributions from both transverse and longitudinal plasmons can be written as [36,62]

$$Q_{\gamma^*} = 2 \int_0^\infty \frac{k^2 dk}{2\pi^2} \frac{\omega \Gamma_{\gamma^*}^T}{e^{\omega/T} - 1} + \int_0^{k_1} \frac{k^2 dk}{2\pi^2} \frac{\omega \Gamma_{\gamma^*}^L}{e^{\omega/T} - 1}, \quad (\text{E2})$$

where the factor of 2 stands for two polarization states of the transverse plasmon, and $\Gamma_{\gamma^*}^{T,L}$ is given by Eq. (E1) with appropriate renormalization factors and dispersion relations. For longitudinal modes, the momentum integration is only allowed upto $k < k_1$. It is defined as the wave number where $\omega(k)$ crosses the light cone, i.e., $\omega/k = 1$,

$$k_1^2 = \frac{3\omega_p^2}{v_*^2} \left[\frac{1}{2v_*} \log \left(\frac{1 + v_*}{1 - v_*} \right) - 1 \right], \quad (\text{E3})$$

where ω_p is the plasma frequency, and v_* is a ‘‘typical’’ electron velocity. For modes above k_1 , the four-momentum of a longitudinal excitation becomes spacelike and are kinematically forbidden to decay.

The photon dispersion relations for a general medium are given by the following transcendental equations [63]:

$$\begin{aligned} \omega^2 - k^2 &= \omega_p^2 \left[1 + \frac{1}{2} G(v_*^2 k^2 / \omega^2) \right], & \text{Transverse} \\ \omega^2 - v_*^2 k^2 &= \omega_p^2 [1 - G(v_*^2 k^2 / \omega^2)], & \text{Longitudinal} \end{aligned} \quad (\text{E4})$$

where ω_p is the plasma frequency, v_* is a ‘‘typical’’ electron velocity, and $G(x)$ is a function defined by

$$G(x) = \frac{3}{x} \left[1 - \frac{2x}{3} - \frac{1-x}{2\sqrt{x}} \log \left(\frac{1 + \sqrt{x}}{1 - \sqrt{x}} \right) \right]. \quad (\text{E5})$$

For highly-degenerate relativistic plasmas, as in our case,

$$\begin{aligned} v_* &\simeq 1, & k_1 &\simeq \infty \\ \omega_p^2 &\simeq \frac{4\alpha}{3\pi} \left(\mu_e^2 + \frac{\pi^2 T^2}{3} \right). \end{aligned} \quad (\text{E6})$$

Let us look at some interesting limits for the dispersion relations in a SN core. At low momentum, $G(x) \simeq 0$ implying $\omega^2 - k^2 = \omega_p^2$ for both transverse and longitudinal modes, while for high momentum modes implying $G(x) \simeq 1$, the dispersion relations have the following form:

$$\begin{aligned} \omega^2 - k^2 &= \frac{3}{2} \omega_p^2, & \text{Transverse} \\ \omega^2 - k^2 &= 0. & \text{Longitudinal} \end{aligned} \quad (\text{E7})$$

Using Eqs. (E7) and (E1), we conclude that for high momentum modes, the decays of longitudinal photon into massive sterile neutrinos become kinematically forbidden for relativistic plasmas. Therefore, the main contribution from longitudinal modes arises from low-momentum modes, but since the production rate depends on k^2 , we expect this contribution to be subdominant to the production through the transverse modes.

The renormalization constants for both transverse and longitudinal modes in highly-degenerate relativistic plasmas are [63]

$$\mathcal{Z}_T = \frac{2\omega^2(\omega^2 - k^2)}{3\omega_p^2\omega^2 + (\omega^4 - k^4) - 2\omega^2(\omega^2 - k^2)}, \quad (\text{E8})$$

$$\mathcal{Z}_L = \frac{2(\omega^2 - k^2)}{3\omega_p^2 - (\omega^2 - k^2)}. \quad (\text{E9})$$

APPENDIX F: PRIMAKOFF SCATTERING

The matrix element for the Primakoff upscattering process $\nu(p_3) + f(p_4) \rightarrow N(p_1) + f(p_2)$, where $f = e^\pm, \mu^\pm, p$ is

$$|\mathcal{M}|^2 = \frac{4d^2 e^2}{q^4} [8(p_1 \cdot p_2)(p_2 \cdot p_3)(p_1 \cdot p_2 - p_2 \cdot p_3) - 2M_N^2(p_1 \cdot p_2 - p_2 \cdot p_3)(p_1 \cdot p_2 + p_2 \cdot p_3 + m_f^2) + M_N^4(p_1 \cdot p_2 - p_2 \cdot p_3 - m_f^2)], \quad (\text{F1})$$

where $q^2 = (p_1 \cdot p_2 - p_2 \cdot p_3)$. Note that for the case of proton, nucleon charge form factor needs to be taken into

account. The form factor $F_1(q^2)$ can be obtained by solving the following pair of equations [12,64]:

$$F_1 - \frac{|q|^2}{4m_p^2} F_2 = G_D, \quad (\text{F2})$$

$$F_1 + F_2 = \mu_{p,\gamma} G_D, \quad (\text{F3})$$

where $\mu_{p,\gamma} = 2.793$ and $G_D = 1/(1 + |q|^2/0.71 \text{ GeV}^2)^2$.

For $\bar{f} + f \rightarrow N + \bar{\nu}$, the matrix element can be obtained using crossing symmetry rules applied to the $|\mathcal{M}|^2$ for $\nu + f \rightarrow N + f$ given above. Since, it is a s -channel process, it does not suffer from singularities unlike t -channel processes.

-
- [1] A. M. Abdullahi *et al.*, The present and future status of heavy neutral leptons, *J. Phys. G* **50**, 020501 (2023).
- [2] A. D. Dolgov, Neutrinos in cosmology, *Phys. Rep.* **370**, 333 (2002).
- [3] P. Coloma, P. A. N. Machado, I. Martinez-Soler, and I. M. Shoemaker, Double-cascade events from new physics in Icecube, *Phys. Rev. Lett.* **119**, 201804 (2017).
- [4] R. Plestid, Luminous solar neutrinos I: Dipole portals, *Phys. Rev. D* **104**, 075027 (2021).
- [5] V. Brdar, A. Greljo, J. Kopp, and T. Opferkuch, The neutrino magnetic moment portal: Cosmology, astrophysics, and direct detection, *J. Cosmol. Astropart. Phys.* **01** (2021) 039.
- [6] V. Brdar, A. de Gouvêa, Y.-Y. Li, and P. A. N. Machado, Neutrino magnetic moment portal and supernovae: New constraints and multimessenger opportunities, *Phys. Rev. D* **107**, 073005 (2023).
- [7] S. N. Gninenko, The MiniBooNE anomaly and heavy neutrino decay, *Phys. Rev. Lett.* **103**, 241802 (2009).
- [8] S. N. Gninenko, A resolution of puzzles from the LSND, KARMEN, and MiniBooNE experiments, *Phys. Rev. D* **83**, 015015 (2011).
- [9] D. McKeen and M. Pospelov, Muon capture constraints on sterile neutrino properties, *Phys. Rev. D* **82**, 113018 (2010).
- [10] M. Masip and P. Masjuan, Heavy-neutrino decays at neutrino telescopes, *Phys. Rev. D* **83**, 091301 (2011).
- [11] M. Masip, P. Masjuan, and D. Meloni, Heavy neutrino decays at MiniBooNE, *J. High Energy Phys.* **01** (2013) 106.
- [12] G. Magill, R. Plestid, M. Pospelov, and Y.-D. Tsai, Dipole portal to heavy neutral leptons, *Phys. Rev. D* **98**, 115015 (2018).
- [13] I. M. Shoemaker and J. Wyenberg, Direct detection experiments at the neutrino dipole portal frontier, *Phys. Rev. D* **99**, 075010 (2019).
- [14] C. A. Argüelles, M. Hostert, and Y.-D. Tsai, Testing new physics explanations of the MiniBooNE anomaly at neutrino scattering experiments, *Phys. Rev. Lett.* **123**, 261801 (2019).
- [15] O. Fischer, A. Hernández-Cabezudo, and T. Schwetz, Explaining the MiniBooNE excess by a decaying sterile neutrino with mass in the 250 MeV range, *Phys. Rev. D* **101**, 075045 (2020).
- [16] P. Coloma, P. Hernández, V. Muñoz, and I. M. Shoemaker, New constraints on heavy neutral leptons from Super-Kamiokande data, *Eur. Phys. J. C* **80**, 235 (2020).
- [17] T. Schwetz, A. Zhou, and J.-Y. Zhu, Constraining active-sterile neutrino transition magnetic moments at DUNE near and far detectors, *J. High Energy Phys.* **07** (2020) 200.
- [18] C. Arina, A. Cheek, K. Mimasu, and L. Pagani, Light and darkness: Consistently coupling dark matter to photons via effective operators, *Eur. Phys. J. C* **81**, 223 (2021).
- [19] I. M. Shoemaker, Y.-D. Tsai, and J. Wyenberg, Active-to-sterile neutrino dipole portal and the XENON1T excess, *Phys. Rev. D* **104**, 115026 (2021).
- [20] A. Abdullahi, M. Hostert, and S. Pascoli, A dark seesaw solution to low energy anomalies: MiniBooNE, the muon ($g-2$), and BABAR, *Phys. Lett. B* **820**, 136531 (2021).
- [21] S. Shakeri, F. Hajkarim, and S.-S. Xue, Shedding new light on sterile neutrinos from XENON1T experiment, *J. High Energy Phys.* **12** (2020) 194.
- [22] M. Atkinson, P. Coloma, I. Martinez-Soler, N. Rocco, and I. M. Shoemaker, Heavy neutrino searches through double-bang events at Super-Kamiokande, DUNE, and Hyper-Kamiokande, *J. High Energy Phys.* **04** (2022) 174.
- [23] W. Cho, K.-Y. Choi, and O. Seto, Sterile neutrino dark matter with dipole interaction, *Phys. Rev. D* **105**, 015016 (2022).
- [24] A. Dasgupta, S. K. Kang, and J. E. Kim, Probing neutrino dipole portal at COHERENT experiment, *J. High Energy Phys.* **11** (2021) 120.
- [25] C. A. Argüelles, N. Foppiani, and M. Hostert, Heavy neutral leptons below the kaon mass at hodoscopic neutrino detectors, *Phys. Rev. D* **105**, 095006 (2022).
- [26] A. Ismail, S. Jana, and R. M. Abraham, Neutrino up-scattering via the dipole portal at forward LHC detectors, *Phys. Rev. D* **105**, 055008 (2022).

- [27] O. G. Miranda, D. K. Papoulias, O. Sanders, M. Tórtola, and J. W. F. Valle, Low-energy probes of sterile neutrino transition magnetic moments, *J. High Energy Phys.* **12** (2021) 191.
- [28] P. D. Bolton, F. F. Deppisch, K. Fridell, J. Harz, C. Hati, and S. Kulkarni, Probing active-sterile neutrino transition magnetic moments with photon emission from CE ν NS, *Phys. Rev. D* **106**, 035036 (2022).
- [29] K. Jodłowski and S. Trojanowski, Neutrino beam-dump experiment with FASER at the LHC, *J. High Energy Phys.* **05** (2021) 191.
- [30] S. Vergani, N. W. Kamp, A. Diaz, C. A. Argüelles, J. M. Conrad, M. H. Shaevitz, and M. A. Uchida, Explaining the MiniBooNE excess through a mixed model of neutrino oscillation and decay, *Phys. Rev. D* **104**, 095005 (2021).
- [31] W. Pauli, Dear radioactive ladies and gentlemen, *Phys. Today* **31**, No. 9, 27 (1978).
- [32] A. Caputo, H.-T. Janka, G. Raffelt, and E. Vitagliano, Low-energy supernovae severely constrain radiative particle decays, *Phys. Rev. Lett.* **128**, 221103 (2022).
- [33] G. Chauhan, S. Horiuchi, P. Huber, and I. M. Shoemaker, Low-energy supernovae bounds on sterile neutrinos, [arXiv: 2309.05860](https://arxiv.org/abs/2309.05860).
- [34] A. Aparici, K. Kim, A. Santamaria, and J. Wudka, Right-handed neutrino magnetic moments, *Phys. Rev. D* **80**, 013010 (2009).
- [35] K. S. Babu, S. Jana, and M. Lindner, Large neutrino magnetic moments in the light of recent experiments, *J. High Energy Phys.* **10** (2020) 040.
- [36] G. G. Raffelt, *Stars as Laboratories for Fundamental Physics* (University of Chicago Press, Chicago, 1996).
- [37] L. Mastrototaro, A. Mirizzi, P. D. Serpico, and A. Esmaili, Heavy sterile neutrino emission in core-collapse supernovae: Constraints and signatures, *J. Cosmol. Astropart. Phys.* **01** (2020) 010.
- [38] S. Hannestad and J. Madsen, Neutrino decoupling in the early universe, *Phys. Rev. D* **52**, 1764 (1995).
- [39] L. Mastrototaro, P. D. Serpico, A. Mirizzi, and N. Saviano, Massive sterile neutrinos in the early Universe: From thermal decoupling to cosmological constraints, *Phys. Rev. D* **104**, 016026 (2021).
- [40] F. Hahn-Woernle, M. Plumacher, and Y. Y. Y. Wong, Full Boltzmann equations for leptogenesis including scattering, *J. Cosmol. Astropart. Phys.* **08** (2009) 028.
- [41] I. Tamborra, L. Huedepohl, G. Raffelt, and H.-T. Janka, Flavor-dependent neutrino angular distribution in core-collapse supernovae, *Astrophys. J.* **839**, 132 (2017).
- [42] G. Martínez-Pinedo, T. Fischer, A. Lohs, and L. Huther, Charged-current weak interaction processes in hot and dense matter and its impact on the spectra of neutrinos emitted from proto-neutron star cooling, *Phys. Rev. Lett.* **109**, 251104 (2012).
- [43] A. Mirizzi, I. Tamborra, H.-T. Janka, N. Saviano, K. Scholberg, R. Bollig *et al.*, Supernova neutrinos: Production, oscillations and detection, *Riv. Nuovo Cimento* **39**, 1 (2016).
- [44] H. K. Dreiner, C. Hanhart, U. Langenfeld, and D. R. Phillips, Supernovae and light neutralinos: SN1987A bounds on supersymmetry revisited, *Phys. Rev. D* **68**, 055004 (2003).
- [45] H. K. Dreiner, J.-F. Fortin, C. Hanhart, and L. Ubaldi, Supernova constraints on MeV dark sectors from e^+e^- annihilations, *Phys. Rev. D* **89**, 105015 (2014).
- [46] A. Caputo, G. Raffelt, and E. Vitagliano, Muonic boson limits: Supernova redux, *Phys. Rev. D* **105**, 035022 (2022).
- [47] P. Carena, G. Lucente, L. Mastrototaro, A. Mirizzi, and P. D. Serpico, Comprehensive constraints on heavy sterile neutrinos from core-collapse supernovae, *Phys. Rev. D* **109**, 063010 (2024).
- [48] O. Pejcha and J. L. Prieto, On The intrinsic diversity of Type II-Plateau supernovae, *Astrophys. J.* **806**, 225 (2015).
- [49] T. Müller, J. L. Prieto, O. Pejcha, and A. Clocchiatti, The nickel mass distribution of normal Type II supernovae, *Astrophys. J.* **841**, 127 (2017).
- [50] J. A. Goldberg, L. Bildsten, and B. Paxton, Inferring explosion properties from Type II-Plateau supernova light curves, *Astrophys. J.* **879**, 3 (2019).
- [51] J. W. Murphy, Q. Mabanta, and J. C. Dolence, A comparison of explosion energies for simulated and observed core-collapse supernovae, *Mon. Not. R. Astron. Soc.* **489**, 641 (2019).
- [52] Garching core-collapse supernova research archive, <https://www.mpa.mpg.de/ccsnarchive/>.
- [53] R. Bollig, W. DeRocco, P. W. Graham, and H.-T. Janka, Muons in supernovae: Implications for the axion-muon coupling, *Phys. Rev. Lett.* **125**, 051104 (2020).
- [54] J. H. Chang, R. Essig, and S. D. McDermott, Revisiting supernova 1987A constraints on dark photons, *J. High Energy Phys.* **01** (2017) 107.
- [55] H. A. Weldon, Simple rules for discontinuities in finite temperature field theory, *Phys. Rev. D* **28**, 2007 (1983).
- [56] G. Lucente, L. Mastrototaro, P. Carena, L. Di Luzio, M. Giannotti, and A. Mirizzi, Axion signatures from supernova explosions through the nucleon electric-dipole portal, *Phys. Rev. D* **105**, 123020 (2022).
- [57] M. Diamond, D. F. G. Fiorillo, G. Marques-Tavares, and E. Vitagliano, Axion-sourced fireballs from supernovae, *Phys. Rev. D* **107**, 103029 (2023).
- [58] M. Diamond, D. F. G. Fiorillo, G. Marques-Tavares, I. Tamborra, and E. Vitagliano, Multimessenger constraints on radiatively decaying axions from GW170817, *Phys. Rev. Lett.* **132**, 101004 (2024).
- [59] A. Caputo, G. Raffelt, and E. Vitagliano, Radiative transfer in stars by feebly interacting bosons, *J. Cosmol. Astropart. Phys.* **08** (2022) 045.
- [60] T. Fischer, S. Chakraborty, M. Giannotti, A. Mirizzi, A. Payez, and A. Ringwald, Probing axions with the neutrino signal from the next galactic supernova, *Phys. Rev. D* **94**, 085012 (2016).
- [61] H. Vogel and J. Redondo, Dark radiation constraints on minicharged particles in models with a hidden photon, *J. Cosmol. Astropart. Phys.* **02** (2014) 029.
- [62] P. Sutherland, J. N. Ng, E. Flowers, M. Ruderman, and C. Inman, Astrophysical limitations on possible tensor contributions to weak neutral current interactions, *Phys. Rev. D* **13**, 2700 (1976).
- [63] E. Braaten and D. Segel, Neutrino energy loss from the plasma process at all temperatures and densities, *Phys. Rev. D* **48**, 1478 (1993).
- [64] D. H. Beck and B. R. Holstein, Nucleon structure and parity violating electron scattering, *Int. J. Mod. Phys. E* **10**, 1 (2001).